

THERMAL EFFECTS OF MATERIAL DISCONTINUITIES AND OXIDATION ON GRAPHITE MATRIX IN HTGRs

Dan Gould, Hanwen Liu, and Hitesh Bindra

Mechanical and Nuclear Engineering

Kansas State University

3002 Rathbone Hall

Manhattan, KS 66506

hbindra@ksu.edu

ABSTRACT

In case of externally initiated events, an HTGR graphite-fuel matrix can experience degradation in passive heat removal capabilities due to development of material discontinuities and changes in radiative emissivities. A packed assembly of cylindrical rods was used for experimentally simulating the impact of material discontinuities during conduction-based passive cool-down at temperatures up to 975 °C. Through the use of an infra-red (IR) camera, high-fidelity thermographic data was obtained from these experiments. This data was then used to train the models for predicting thermal response for graphite and alumina materials. The supervisory models were used to predict thermal behavior in other experiments with different operational conditions. When trained with the optimal thermographic data, the normalized error magnitudes from these model predictions were less than 1%.

Graphite-fuel matrix in HTGRs can come in direct contact with air at high temperature during air ingress associated with severe accidents, which can affect their passive heat removal capabilities. Nuclear grade graphite has been shown to undergo oxidation when subjected to an air ingress at high temperatures, potentially resulting in density changes near the surface. The oxidation process can have a substantially negative impact on the thermal properties of graphite such as thermal conductivity and emissivity, which in turn can eventually lead to higher core temperatures. The qualitative and relative effects of oxidation on graphite emissivity have been reported.

KEYWORDS

HTGRs, Air ingress, emissivity, Gap conductivity

1. INTRODUCTION

The severe accident at the Fukushima Daiichi Nuclear Power Plant made clear that increased investigation of the responses of nuclear facilities to externally or environmentally initiated events, such as strong earthquakes, tsunami or other mechanical shocks, is needed. Due to both the uncertain consequences of these events and to public concern, inherently safe reactors or reactors with passive safety design are paramount to the future of nuclear energy in the world. The next generation of nuclear power plants, such as HTGRs, have been designed to possess significant number of passive safety features. However, it is unclear whether their safety systems will perform as per design requirements in case of externally initiated events. In these reactors, it is of primary importance that the decay heat be removed to the Reactor Cavity Cooling System (RCCS) under all circumstances.

The integrated examination of reactor systems and passive heat removal systems under seismic activity or similar external impact will require the construction of a highly advanced, pilot-scale demonstration facility, capable of both inducing mechanical shocks and possessing re-usable capability. The design and construction of such a sophisticated facility – which should include monitoring of seismic responses of RCCS as well as a complete reactor system – will require significant resources. Therefore, a practical approach is to improve the understanding of this multi-physics problem computationally and validate computational models with separate effect experiments.

Passive decay heat removal is one of the prime passive safety, or inherent safety, features of HTGRs. The HTGRs are designed to provide long-term heat removal via conduction, natural convection and radiation heat transfer modes during loss of forced circulation of reactor coolant (Helium) in Pressurized Conduction Cool-down (PCC) or Depressurized Conduction Cool-down (DCC) scenarios. However, if severe accidental situations arise due to mechanical shocks, it may damage the brittle graphite-fuel matrix such as in case of prismatic fuel blocks of Very High Temperature Reactors (VHTRs). The damaged prismatic blocks will negatively impact the natural circulation and may result in the degradation of effective thermal conductivity of the graphite-fuel matrix due to additional gaps. The diagram depicting the impact of such severe accidents on the core geometry is presented below as Figure 1.

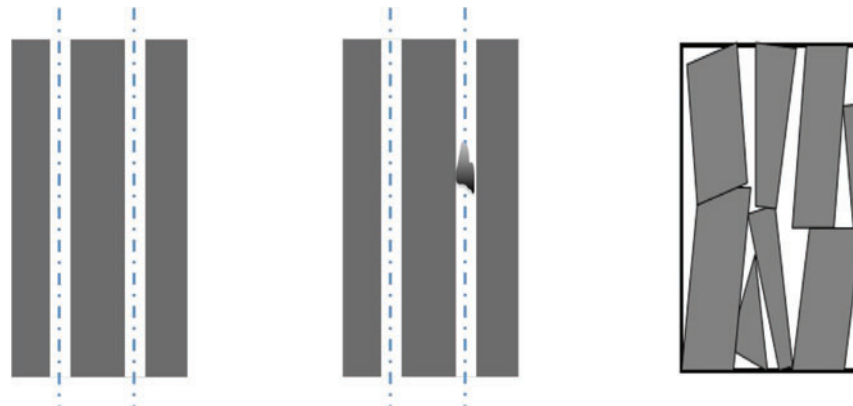


Figure 1. (Left to Right) Section of VHTR prismatic block showing cylindrical regular channels for flow of coolant; severe accident hypothesis with debris blocking the coolant flow path; and severely damaged blocks leading to thermal discontinuities and gaps in prismatic blocks.

A primary concern in the event of an air-ingress resulting from a break in the coolant system is the potential of the near-surface graphite to oxidize resulting in the degradation of its thermal properties. This can eventually give rise to thermal instabilities and even potentially trigger conditions in which the safety envelope of the TRISO fuel may be breached. According to Phenomena Identification and Ranking Tables (PIRT) for VHTRs [1-4] under normal steady-state, transient, and accident scenarios, air ingress is one of the key phenomena leading to localized hot spots in the reactor core and heat transfer degradation in coolant channels. Chang Oh et al. [5] performed computational fluid dynamics simulations on effect of air ingress on natural circulation in VHTRs. The graphite oxidation due to air ingress in HTGRs at higher temperatures has been studied computationally [6]. However there are limited experimental data on the effect of air or steam ingress on thermal properties of nuclear graphite post-oxidation at high temperatures or severe accident situations. Schweitzer[7,8] conducted airflow experiments in heated graphite channels to investigate graphite rapid oxidation mechanisms and possibilities. The oxidation studies for nuclear grades of graphite have been conducted, but most of these studies were limited to the chemical reaction kinetic temperature regime. Some graphite-oxygen oxidation experiments conducted up to 1600°C have shown that at higher temperatures graphite oxidation is limited by supply of oxidant to the Reactive Surface Area

(RSA) [9-11]. In addition, surface analysis and penetration depth studies of the oxidized graphite samples at lower oxidizing temperatures (500-800°C) have shown considerable change in the surface topology, pore structure within the graphite material and led to considerable reduction in density up to penetration depth of 3-4 mm. In addition, these effects can lead to considerable changes in near-surface thermal properties of graphite such as emissivity. Figure 2 is provided below as an example of some of the potential changes in surface properties which can be attributed to oxidation. Here, the oxidation is shown to radically change the color and emissivity of a typical graphite sample that suffers from a higher degree of impurities.

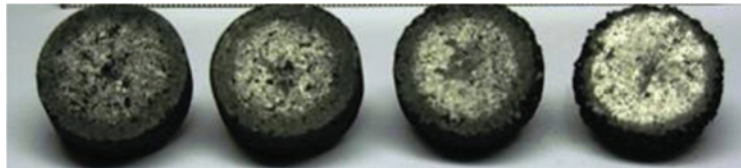


Figure 2. Surface of graphite coupons exposed to oxidation environment at high temperature. Outer edges were not exposed due to presence of ceramic clamps [12].

Although nuclear graphite is purified to total impurity levels below 300ppm, it is anticipated that over the lifetime of the reactor some of these impurities will eventually be oxidized and form a light ash deposit on the outer surface of the graphite components. These oxidized impurities exhibit a light grey color, which can reduce the emissivity and heat transfer efficiency from the purely black carbon-only surface of the graphite components.

One of the objectives of this study was to experimentally observe and understand the effect of material discontinuities, such as in case of line-to-line contact, on overall heat conduction process. Second objective was to observe and measure changes in the graphite emissivity in high temperature oxidation events. This paper provides details of the design, construction, and capabilities of a custom experimental apparatus to estimate effective thermal properties of a graphite and ceramic material matrix, along with high fidelity thermographic experimental results. The created experimental setup was shown to be capable of thermographically examining material samples at temperatures higher than 1250 K in a number of operational environments. The analysis methods and data learning methodology for future experiments is also documented.

2. EXPERIMENTAL SETUP

2.1. Design Motivation

The goal of utilizing modern thermographic methods to study the oxidation behavior of graphite at high temperatures led to the formulation of several distinct requirements for the design of the experimental setup. It was required that the experimental infrastructure possess the ability to heat graphite and any other desired test specimen to temperatures higher than 450 °C; i.e. above the minimum temperature at which graphite oxidation can be practically observed when exposed to air. The majority of previously undertaken studies have shown substantial changes in the graphite surface topology and near surface density at temperatures 500- 800 °C. Therefore, the target was established to conduct experiments up to 900 °C, or 1173 K. The need for both experimental controls and experimental repeatability necessitated the ability to precisely control the fluidic environment around the tested sample piece. This requirement entailed the setup possessing the ability to operate in both above atmospheric pressures and vacuum environments.

Finally, as it was desired to utilize thermographic methods to assist in the high-resolution characterization of graphite at these high temperatures, the designed system had to have a window and/or optical system to

allow the transmission of infrared radiation. Modern thermographic cameras provide the ability to measure the spatial variation of temperature upon a surface at a much higher resolution than almost any other temperature measurement method[13]. In this work, the FLIR A665sc camera was used. Due to the use of this particular camera, the requirement of an optical system capable of transmitting IR radiation was further defined by the subset of wavelengths – that is, wavelengths of 8 - 13 micron – detected by the available thermographic camera.

In addition to the high resolution, the use of the IR camera i.e. a non-invasive technique also led to simpler experiment design. First, by eliminating the need for contact temperature devices, no thermocouple feedthroughs were needed for the flow chamber. Additionally, the lack of measurement devices within the chamber allowed for the size of the test pieces to be maximized. Even more importantly however, the non-contact nature of the IR camera released the designer from onerous requirements of attaching a contact temperature measurement device to the surface of a potentially oxidizing and degrading test pieces without either affecting either the surface of the test piece or the accuracy of the measurement. The test pieces used in these experiments were cylindrical rods of graphite and alumina, and more details are provided in the next section on experimental procedure.

2.2. Setup Design

The test chamber was built and housed inside a tube furnace with operating temperature limits higher than 1373 K within its 75mm diameter cavity. Several materials were considered for process tubes, and quartz tube was selected as its low thermal conductivity resulted in low enough temperatures at the ends of the tube for it to be sealed with O-rings. In addition, due to fused quartz being transparent to thermal radiation of wavelengths as high as three microns, using a quartz process tube also allowed for very effective radiative heating of the test samples at high temperatures where the majority of the thermal energy from the furnace transmitted through the quartz process tube and into the test pieces.

The compression fittings were used to both seal each end of the quartz process tube and allow for connections to be made to both vacuum pumps and pressurized gas cylinders. Finally, a custom ZnSe window was designed, machined and built so that a long wave IR camera could be used to collect the temperature maps of the test pieces during the oxidation process and thermal conductivity of the test pieces. While commercial ZnSe viewports are widely available, the custom solution used in the described experimental setup was created at a fraction of the price of purchasing a premade window. The resulting set up was able to fulfill all of the outlined design requirements. In this setup, samples up to .3 m long and 47 mm in diameter can be studied at temperatures up to 1373 K in either vacuum or pressurized environments featuring overpressures greater than 150 kPa.

In addition to the static environment testing capabilities mentioned above, space, support, and access points were included at the ends of the process tube to allow for simple modification of the current system to allow for dynamic flow simulations as well. A simplified version of the completed setup can be seen in Figure 4 while the entire final construction is presented in IR in Figure 3.

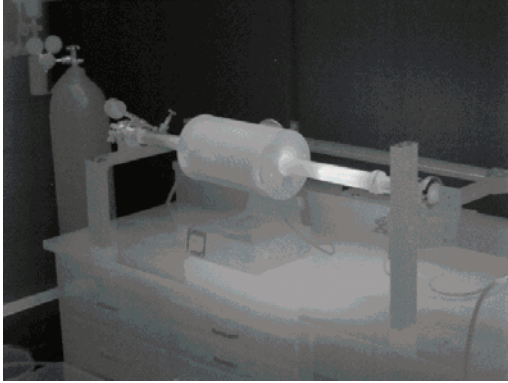


Figure 3. Infrared image of completed experimental setup

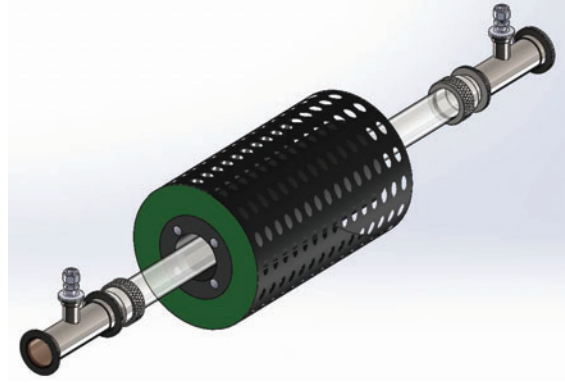


Figure 4. CAD depiction of experimental setup

3. EXPERIMENTAL PROCEDURES

3.1. Conduction Cool-Down: Effects of Material Discontinuities

The assembly of test pieces, i.e. seven cylindrical rods of diameters 15.24 mm (.6 in) and lengths 152.4 mm (6 in), was placed inside the quartz process tube. This resulted in near optimal packing efficiency and near uniform contact between each rod. The length to diameter ratio of the test pieces was based on material availability. The packing methodology used was chosen to experimentally simulate the effect of ordered material discontinuities.

A diagram depicting the cross-sectional view of this assembly is shown below in Figure 5. Numbers are inscribed on each of the outer rods for ease of individual identification in future references. The rods were carefully aligned so that each one was located an equal distance into the process tube and were positioned so that the target faces were approximately 0.270 m from the ZnSe window attached to the end of the tube. This location was found to be optimal based on two factors.

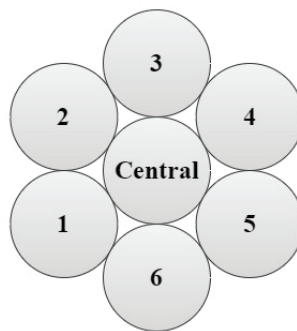


Figure 5. Diagram of assembled bundle of test pieces as seen by the thermographic camera

First, the minimum focal length of the optics attached to the thermographic camera was 0.25 m. As optimal resolution of the test pieces would only be achieved if the target faces were located at precisely this location from the camera, it was of course desired to place the cylinders as close to this mark as possible. Due to the width of the fittings sealing the quartz process tube, achieve this exact distance would have required placing

the test pieces extremely close to the end fittings. However, as the rods were to be heated in a tube furnace, the placement of the test pieces was also limited by the thermal limitation of both the camera and the tube seals. Thus the rods were placed at the closest possible location allowable by the thermal loads imposed by the furnace on the fittings and camera.

Once the rods were sealed in the process tube, the air within the tube was evacuated until a full rough vacuum was reached. That is, the chamber was evacuated to a point somewhere below the measurement ability of a standard bourdon differential pressure gauge. The tube furnace was then moved along the process tube so that the face of the rods were located just inside the heated section of the furnace – approximately two inches from the furnaces outer edge. The furnace was then switched on and allowed to heat the rods to the desired temperature.

For conduction cool-down experiments, when the test pieces were shown by the thermographic camera to have achieved steady state conditions at the desired temperature, the tube furnace was quickly turned off and slid away from the test pieces down to the other end of the 1.22 m process tube. While located at the opposite end of the process tube, although the interior of the furnace remained at a high temperature, the view factor of the heater as seen by the test pieces was negligible. This process took on average 4 seconds to perform, which, due to the much larger time scale of the overall cool-down experiment, was judged to be sufficiently short as to not affect the results in any way. The desired steady state temperatures can be referred to as initial temperatures for cool-down experiments.

The camera was then used to track each rod's change in temperature as each lost stored thermal energy via conduction and thermal radiation through the quartz tube where the heat was removed into the room via natural convection. While radiative losses from the outer rods to the quartz tube might be of significance during the initial stages of the cooling process, as the method of quantitative analysis used in this paper does not require an exact evaluation of the different modes of heat removal, no further discussion of this possibility is provided within this work. The aforementioned experimental procedure was performed for both alumina and graphite test pieces over a range of initial temperatures varying from 773 K to 1250 K. All of these experiments were performed in rough vacuum environments.

3.2. Graphite Oxidation, Emissivity Changes and Material Degradation

A second group of experiments was performed in a combination of different environments which allowed partial to full oxidation on the target faces. These controlled experiments were conducted with the goal of obtaining a better understanding on the graphite oxidation conditions and their effects on emissivity of graphite.

Initially, a new set of graphite test pieces were sealed into the quartz process tube and heated to 1250 K while subjected to a full rough vacuum. That is, the chamber was evacuated to a point somewhere below the measurement ability of a standard bourdon differential pressure gauge. By repeating this experiment with a new set of graphite rods and comparing the results with those generated by the previous test pieces it was possible to determine whether the repeated thermal cycling of the graphite in the previous experiments had caused any changes in the material despite the vacuum environment.

Later, the graphite rods were then raised to and held at 1250 K at decreasing levels of vacuum. Over the course of four repetitions, the pressure within the process tube was raised from full rough vacuum to 1.0 atm. During each of these runs, the graphite was brought to 1250 K and held there while being carefully watched for any signs of oxidation and/or material degradation using IR camera.

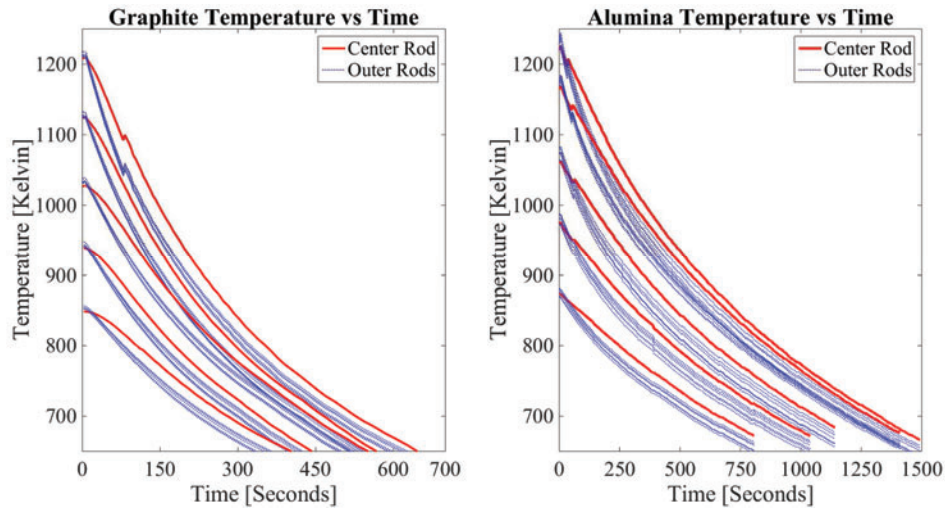
For the final test, graphite rods were subjected to 1250 K while being held partially outside of the process tube. In this experiment the rods were subjected to an oxidizing environment and natural air currents in an

attempt to allow the maximum effects of oxidation (without forced convection) to be examined. These tests were performed with the CO and CO₂ sensors in close proximity for safety purposes.

4. RESULTS AND DISCUSSION

4.1. Cooling via Conduction and Effects of Material Discontinuities

Figures 6 and 7 respectively, present the rate of temperature change with time observed for the graphite and alumina as they were cooled. Each of the solid red lines in this plot represent the change in average temperature of the central rod within the test assembly while dotted blue lines are used to display the average temperatures of each of the surrounding rods. As anticipated, the temperature profiles plotted in Figure 6 show very good agreement with one another as the overall shape remains nearly constant and simply scaled by the initial temperature of the rods. Similarly, the alumina cooling profiles in Figure 7 also show good agreement with each other.



Figures 6 and 7. Alumina and graphite temperature variation with time

While both Figures 6 and 7 at first glance seem to have similar trends, this is almost entirely due to scaling. These differences are more easily seen in Figure 8, below. For this figure, the average temperatures of the central rods from each set of tests were non-dimensionalized using Equations 1 and 2.

$$t^* = \frac{t}{t_{\max(T_0)} \Big|_{T=650K}} \quad (1)$$

$$q = (T_{\max} - T_{ave})(T_{\max} - T_{min})^{-1} \quad (2)$$

Figure 8 clearly shows the large differences between the rates at which the two different materials are cooling. This difference is a result of two different factors. First, due to a large difference in the densities of the two materials, the alumina test pieces were capable of storing more energy at a given temperature despite their lower specific heat [14,15]. Over a temperature rise of 800 K, this resulted in the alumina being able to store 30% more thermal energy than the graphite. Secondly, due to the axially uneven temperature distribution of the furnace used to heat each test assembly combined with the decreasing

thermal conductivity of alumina at high temperatures, it is likely that although the face of the rod facing the camera was at the specified temperature, the rod's axial temperature distribution was not uniform. Thus, the value of the average volumetric temperature could be significantly higher for the alumina rods than for those made out of graphite even if they were both found to possess equal temperatures at their respective faces.

Second, due to the diameter and straightness tolerances of the tested alumina being larger than those of the obtained graphite, the packing of the rods into the process tube did not result in as perfect a fit. These small gaps introduced a significant thermal resistance in the radial direction. An effect of this packing inefficiency can be seen in Figure 8 where the difference between the center rod and outer rod temperatures for the alumina test pieces is significantly larger than that allowed by the graphite assembly.

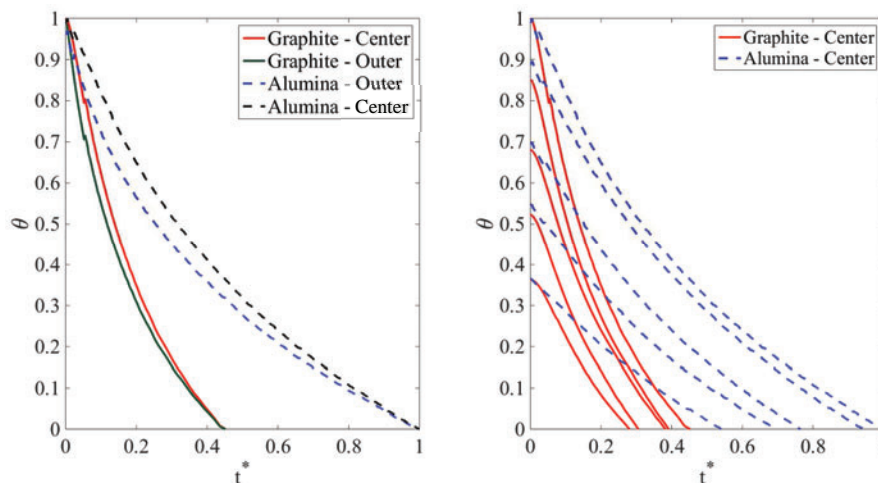


Figure 8. Temporal variation of non-dimensional temperature of graphite and alumina samples

Further analysis on the results from the alumina and graphite cooling studies was performed to develop an ‘operator’ that, given the temporal data obtained from cooling the assembly from one set of initial temperatures, would be able to predict thermal behavior of the assembly if it were to be later cooled with different set of initial temperatures. As can be seen in the schematic of test assembly, the outer rods 1-6 are directly touching the quartz tube. These rods therefore directly conduct their thermal energy to the quartz, which almost immediately drops to a much lower temperature when the heater is removed. In contrast to this, the center rod is almost completely surrounded by outer rods and thus rejects heat only via gap thermal conduction along the line-to-line interaction with outer rods. Heat conduction across the gaps in such arrangements is difficult to model and then validate using experimental data. Thus, thermographic images during cooling down experiments are aimed to generate this high accuracy ‘operator’.

The ‘operator’ is based on supervised learning with the help of the temperature response data of the center rod as a function of temperatures of the outer rods. The data trained ‘operator’ can be mathematically expressed in the manner shown by Equation 3. In this equation, \hat{T}_c and T_c are, respectively, the predicted and actual spatially-averaged center rod temperatures at any instant. The variable T_i is defined as the spatially-averaged instantaneous temperature for one of six outer rods. The coefficients $w = (w_0, w_1 \dots w_6)$ can be obtained by least square minimization of errors. An example of this is given in Equation 4. The resulting predicted temperature values for the center rod obtained through the use of this ‘operator’ and their comparison with actual measurements can be seen below in Figures 9 and 10.

$$\hat{T}_c(w, T_i) = w_0 + \sum_{i=1}^6 w_i T_i \quad (3)$$

$$\min_w \|T_c - \hat{T}_c\|_2^2 \quad (4)$$

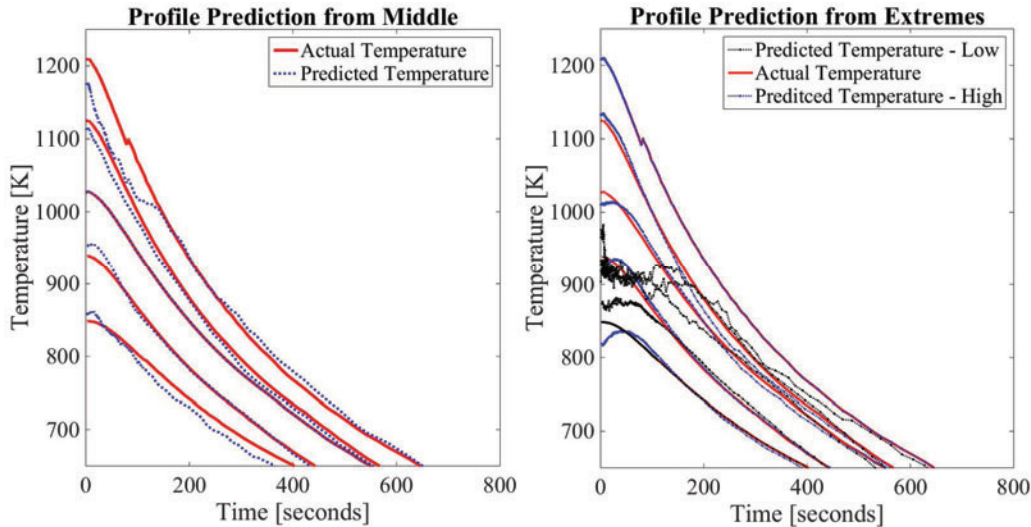


Figure 9. Predicted vs actual center rod temperature profiles – Graphite

As the coefficients for the ‘operator’ can be obtained by using the input from the temporal center rod temperature data from any of the runs, the two plots making up Figure 9 are used to display the variation in the predictability of the ‘operator’ based on what input it receives. The left plot of Figure 9 displays the predicted temperatures against the actual temperatures in the case where the data resulting from cooling from a mid-range temperature are input into it. As one would expect, the ‘operator’ is able to predict the temperature profile of the profile it is given perfectly. It also performs relatively well at predicting the temperature profiles for the experiments which did not provide the training temperature data for the formulation of operator.

The plot displayed on the right side of Figure 9 presents the output from the ‘operator’ when the data from the highest and lowest temperature tests. This time, while the ‘operator’ is very effective at predicting the temperature profile when fed the data from the highest temperature experiment – obtaining predictions with a maximum error of less than 3.8% and generating profiles with median errors of less than 1% in all cases – it is thoroughly unable to predict the cooling profiles of the higher initial temperature runs when given data from the cooling experiment with the lowest initial temperature.

Similar levels of ‘operator’ accuracy are seen for alumina in Figure 10. The ‘operator’ obtained using data from the runs with the middle or highest initial temperatures is quite successful at predicting the temperature profiles of each of the other experiments. However, once again the ‘operator’ developed using data from the test with the lowest initial temperature fails to be even moderately successful in attempts to predict the thermal profiles of the higher initial temperature experiments.

The evidence of the primacy of the error caused by a lack of signal definition at lower temperatures is found by comparing the predictions of graphite centerline temperatures resulting from the use of the highest and middle initial temperature values. Although the average magnitude of the difference between input data and

the correct value was larger when the highest temperature data was used as an input, the predicted values returned by the ‘operator’ were actually more accurate than those given when the middle temperature profile is provided as input. This fact also further reinforces the value of the experimental setup described within this work. Due to the high temperatures it is able to operate at, any ‘operator’ created by data generated within said setup will likely be able to extrapolate down from high temperature experimental results and avoid the large errors seen by doing the opposite in Figures 9 and 10.

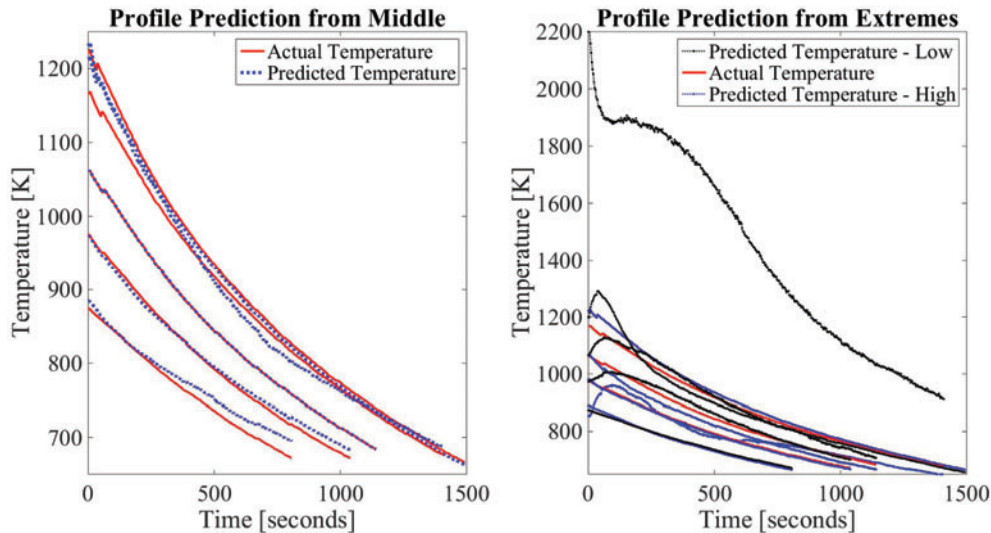


Figure 10. Predicted vs actual center rod temperature profiles – Alumina

4.2. Graphite Oxidation and the Effects on Emissivity

When the experimental methodology described within this work was conceived, it was assumed that simply holding a rough vacuum around the graphite test rods would be sufficient to prevent any oxidation from occurring when it was exposed to high temperatures. In the course of gathering the requisite data for the aforementioned transient cooling study, the graphite test pieces were repeatedly heated to temperatures higher than 1250 K. This value is well above the temperature at which the graphite grade used is known to begin to oxidize when surrounded by an oxidizing environment[16]. Thus, tests were undertaken to ensure that if any oxidation had occurred despite the vacuum, it was of such a minor scaled that it could be negated. One of the results of these tests is shown in Figure 11, below, where the centerline temperature of a graphite test piece is plotted while it cools in an oxidizing and a sealed oxidizing environment. Due to the extreme similarity between the two plotted profiles, it is fair to assume that simply existing in an oxidizing environment is not enough to allow significant oxidation to occur over the time scale of the experiment.

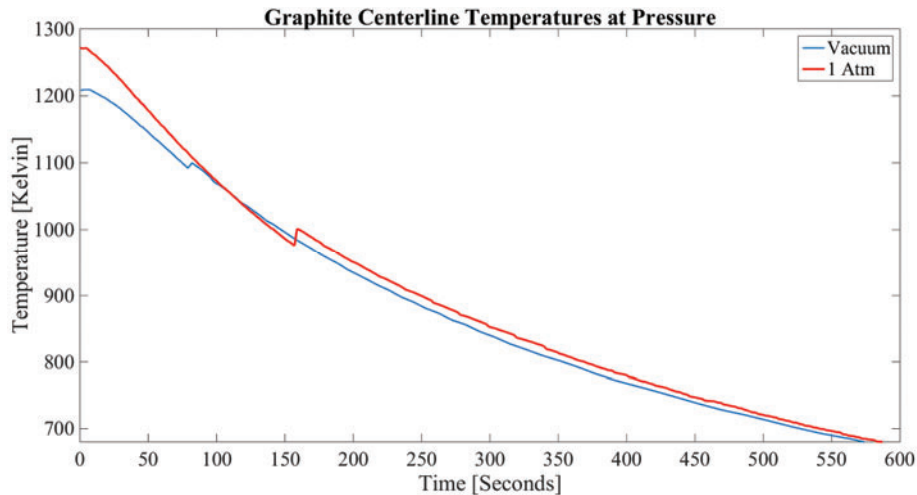


Figure 11. Centerline temperature while in sealed environment at atmospheric pressure.

Therefore the graphite rods were half removed from the end of the process tube and placed into the furnace completely exposed to atmosphere and any flows within it. It was during this experiment that large amounts of oxidation were observed. Examples of such oxidation can be seen in Figure 12 where three images captured by the camera 0.16 seconds apart are displayed. In each of these frames vast differences can be seen between the face temperatures of some of the rods with some rods reporting on the order of 100 K over their neighbor rod. However, rather than being an accurate description of the temperature difference between two rods, this incorrect reading is almost entirely due to the growth of an oxide layer on the faces of some of the rods. The IR camera displayed temperature maps based on a spatially constant emissivity value, thus the effect of emissivity variation due to oxidation can be visualized as apparent differences in temperatures. In Figure 12, the three displayed images are taken from immediately before, during, and immediately after the detachment of a flake of the oxide layer that had grown on the surface of the graphite. The rods on which a complete oxide layer has formed can be identified in Figure 12 by their green – rather than orange – appearance.

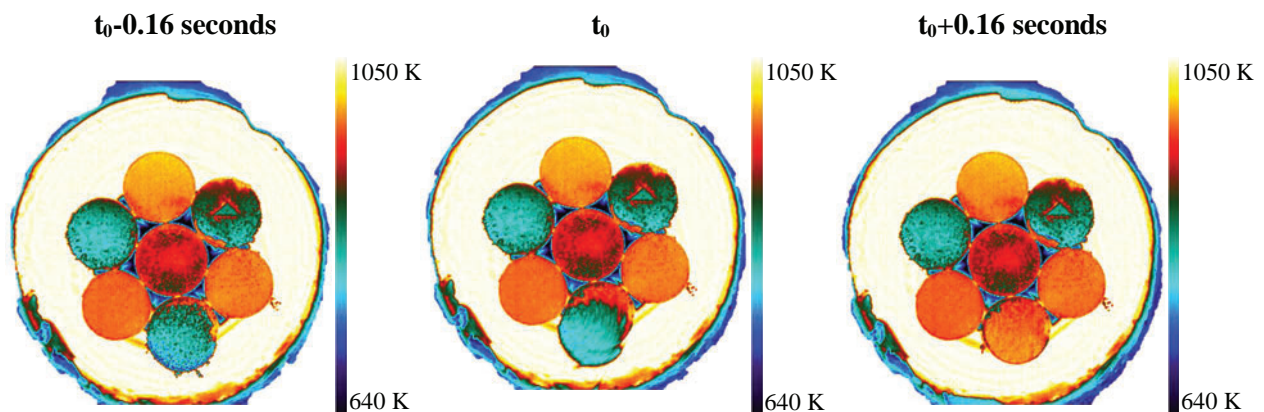


Figure 12. Images of oxidized graphite before, during, and after oxidized layer releases from graphite face.

The plot shown in Figure 13, below, is an approximate calculation for the ratio of the average emissivities between outer rods one and two. This value is plotted over a chosen time period of interest during the initial

heating of the graphite test pieces while they were exposed to the atmosphere. The x-axis reference point $t_o = 0 \text{ sec}$ was set to be equal to the time of the frame shown in Figure 12 in which the flake detached from the rod. At this point in time, the ratio of emissivities plotted in Figure 13 suddenly increases by about 50%. The timing of this jump perfectly coincides with the detachment of the oxide layer from the face of the rod as shown in Figure 12. Therefore, it can be safely concluded that the variation in rod temperature seen by the camera and shown in Figure 12 is indeed due to the spatially and temporally varying emissivity caused by the formation of oxide layers on the surface of the graphite rods.

For this calculation, it was assumed that both the average temperature and cross-sectional area of each rod were identical and did not vary temporally during the specified time period during which the measurement was taken. The IR camera was set to record 6.25 frames per second, which resulted in a measurement time of .16 seconds. With these assumptions, any temperature differences observed between these two rods would therefore be the direct result of differing emissivities. Indeed, analysis of Figures 12 and 13 provides confirmation that, in an oxidizing environment, variations in emissivity far and away become the dominating factor in apparent temperature differences between outer rods.

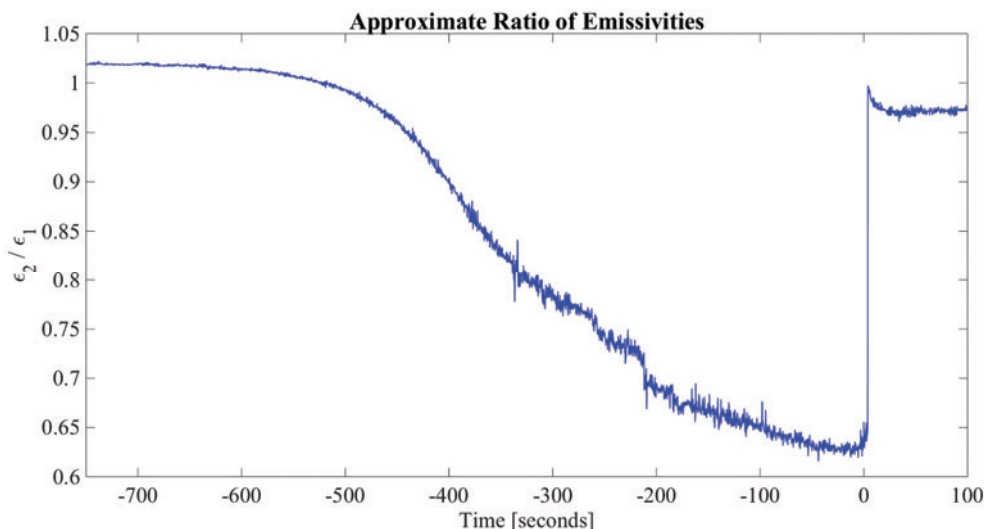


Figure 13. In this figure an approximation for a ratio between the emissivities of two of the outer rods.

The following two visible-light camera pictures presented in Figure 14 show the effects of the high temperatures and oxidizing environment on the graphite test pieces. As it is clearly seen in the picture, the rods that were heated in an oxidizing environment suffered significant degradation. This provides visual demonstration of the ability of oxidation to not only degrade the graphite's emissivity, but also can decrease the thermal conductivity of a material by increasing the size of any cracks or crevices already existing in said material. One point of interest that should be mentioned is the abrupt halt to the material degradation seen to occur approximately halfway along the axial length of each of the exposed rods in Figure 14. This sudden change in shape marks depth to which the graphite test rods were inserted into the quartz process tube during oxidation experiment. While technically the entire surface of each of the tested rods were exposed to an oxidizing atmosphere, simply being covered by the glass was enough to prevent the flow conditions that would cause rapid and significant oxidation to occur on curved surfaces of the test pieces.



Figure 14. Top and side views of two assemblies of graphite test pieces demonstrating the effects of oxidation.

It should be noted here that as the focus of this work was to establish techniques for – as opposed to generating narrowly applicable data from – quantitative and qualitative measurements for high temperature graphite experiments, it was decided that the significantly increased experimental repeatability enabled by using a markedly more cost effective grade of graphite, POCO-EDM3, would be of greater overall benefit than the increased applicability that would have resulted from obtaining similar test pieces of a nuclear grade graphite. While the bulk material properties of high purity pyrolytic graphite at the beginning of life are firmly documented, it is reasonable to assume that over the course of its lifetime within a reactor the quantity of impurities in the graphite, although initially very low, will increase. Therefore, the results obtained in this study can be looked at as a limiting case that would be approached as impurities become present within actual reactor graphite whether due to age or manufacturing defect.

5. CONCLUSIONS

The effects of ordered material discontinuities on the conduction cool-down were experimentally simulated. The thermographic data based modeling of gap thermal conductivity led to the formation of data training ‘operator’. The predictability of data trained ‘operator’ to estimate the temperature across material discontinuities was examined for experiments performed at different temperatures. The predictions were found to be in good agreement with measurements in wide range of experiments when the ‘operator’ was trained with the response data from the high temperature experiments. In particular, when input with the temperature response data from the trial where the graphite test pieces were cooled from the highest initial temperature it was able to predict all other temperature profiles with a mean error of less than 1% in every case. However, when trained using data from low initial temperature experiments, the ‘operator’ did not perform as well in predicting the temperature profiles actually obtained by the other, higher temperature experiments.

Finally, rather than simply being a function of only temperature, it can be concluded from this work that the oxidation process of graphite requires a non-negligible flow of oxidizing material along the surface of the sample for any significant amount of oxidation to occur. This result was confirmed twice in this investigation. First, it was shown that heating even commercial grade graphite in a stationary, slightly oxidizing environment was not enough to oxidize the rods quickly enough to change the results to something different than that of the previous experiments. Further reinforcement of this conclusion can be found by visual inspection of the images comparing the graphite exposed to an oxidizing fluid flow to that which was not. In these images, a sudden halt in material degradation along the surface of the outer rods can be seen at the exact axial position equal to the depth to which the assembly was inserted into the quartz process tube. As the portions of the test pieces within the quartz tube were subject to equal or greater thermal loads – but less oxidizing fluid flow – than the exposed parts, this correlation between the depth of insertion and length of portion of the rods suffering significant material degradation provides additional evidence of the significance of fluid flow in the oxidation of graphite.

REFERENCES

1. R. Vilim, W. Pointer and T. Wei, "Prioritization of VHTR System Modeling Needs Based on Phenomena Identification, Ranking and Sensitivity Studies," *ANL-GenIV-071*(2006).
2. R. R. Schultz, P. D. Bayless, R. W. Johnson, W. T. Taitano, J. R. Wolf and G. E. McCreery, *Studies Related to the Oregon State University High Temperature Test Facility: Scaling, the Validation Matrix, and Similarities to the Modular High Temperature Gas-Cooled Reactor*(2010).
3. R. R. Schultz, A. M. Ougouag, D. W. Nigg, H. D. Gougar, R. W. Johnson, W. K. Terry, C. H. Oh, D. W. McEligot, G. W. Johnsen, G. E. McCreery, W. Y. Yoon, J. W. Sterbentz, J. S. Herring, T. a Taiwo, T. Y. C. Wei, W. D. Pointer, W. S. Yang, M. T. Farmer, H. S. Khalil and M. a Feltus, *Next Generation Nuclear Plant Methods Technical Program Plan*(2007).
4. S. J. Ball and S. E. Fisher, *Next Generation Nuclear Plant Phenomena Identification and Ranking Tables (PIRTs)* (2007).
5. C. H. Oh, H. S. Kang and E. S. Kim, "Air-ingress analysis: Part 2—Computational fluid dynamic models," *Nuclear Engineering and Design*, **241**(1), pp. 213–225 (2011).
6. Y. M. Ferng and C. W. Chi, "CFD investigating the air ingress accident for a HTGR simulation of graphite corrosion oxidation," *Nuclear Engineering and Design*, **248**, pp. 55–65 (2012).
7. D. G. Schweitzer, "Oxidation and Heat Transfer Studies in Graphite Channels: I. The Effect of Air Flow Rate on the CO₂ and CO-O₂ Reactions," *Nuclear Science and Engineering*, **12**(1), pp. 49–45 (1962).
8. D. G. Schweitzer and D. H. Gurinsky, "Oxidation and Heat Transfer Studies in Graphite Channels - II. Thermal Changes With Time and Distance in Air-Cooled Graphite Channels," *Nuclear Science and Engineering*, **12**, pp. 46–50 (1962).
9. W. Windes, G. Strydom, R. Smith and J. Kane, *Role of Nuclear Grade Graphite in Controlling Oxidation in Modular HTGRs*(2014).
10. J. J. Lee, T. K. Ghosh and S. K. Loyalka, "Oxidation rate of nuclear-grade graphite NBG-18 in the kinetic regime for VHTR air ingress accident scenarios," *Journal of Nuclear Materials*, **438**(1), pp. 77–87 (2013).
11. J. J. Lee, T. K. Ghosh and S. K. Loyalka, "Oxidation rate of nuclear-grade graphite IG-110 in the kinetic regime for VHTR air ingress accident scenarios," *Journal of Nuclear Materials*, **446**(1-3), pp. 38–48 (2014).
12. W. Windes, 2014, NGNP Graphite R&D Technical Lead, Idaho National Labs, private communication.
13. M. Patel, K. Saurabh, V. V. B. Prasad and J. Subrahmanyam, "High temperature C / C – SiC composite by liquid silicon infiltration :," **35**(1), pp. 67–77 (2012).
14. Y. S. Touloukian, "Specific Heat: Nonmetallic Solids," *Thermophysical properties of matter*, v. 5, Plenum(1970).
15. G. T. Furukawa, T. B. Douglas, R. E. McCoskey and D. C. Ginnings, "Thermal properties of aluminum oxide from 0 to 1200 K," *Journal of Research of the National Bureau of Standards*, **57**(2), p. 67 (1956).
16. D. M. Sheppard, R.G., Morgan, Dqayne, Mathes, *Properties and Characteristics of Graphite For the EDM Industry*(2002).